Electrochemistry Communications 108 (2019) 106578

Contents lists available at ScienceDirect

Electrochemistry Communications

journal homepage: www.elsevier.com/locate/elecom

H_2 permeation through N117 and its consumption by IrOx in PEM water electrolyzers

Georgios Papakonstantinou[a,*], Kai Sundmacher[a,b]

[a] Max Planck Institute for Dynamics of Complex Technical Systems, Process Systems Engineering, Sandtorstr. 1, D-39106 Magdeburg, Germany
[b] Otto-von-Guericke University, Process Systems Engineering, Universitätsplatz 2, D-39106 Magdeburg, Germany

ARTICLE INFO

Keywords:
PEMWE
H_2 permeation
H_2 consumption
Mass transport
Tafel slope
IrOx oxyhydroxides

ABSTRACT

It is considered that the oxidation activity of Ir based anodes on H_2 permeating the polymer electrolyte membrane (PEM) in PEM water electrolyzers (WE) is poor, resulting in high H_2-in-O_2 contents at idle or dynamic operating conditions, especially with asymmetric pressure. In the present work, the dependence of H_2 permeation on cathode pressure was quantified by the pressure drop method. H_2 consumption was detected by chronoamperometry at potentials preceding water splitting. The addition of N_2 in the anode outlet gas allowed the on-line monitoring of the mixture composition during idle PEMWE operation by a thermal conductivity sensor. It is found that H_2 is effectively consumed with IrOx oxyhydroxide anodes at low current densities, with 75% conversion of the zero-current permeation at cathode pressure of 5 bar and 60 °C. Hence, both H_2-in-O_2 content and lowest current density at which the H_2-in-O_2 flammability limit is not exceeded decrease by more than 50%. Current density corrections accounting for H_2 consumption and mass transport potential corrections accounting for the enhancement of H_2 permeation with current density were implemented. The resulting Tafel slope values suggest that the rate determining step of the oxygen evolution reaction with IrOx oxyhydroxides is a chemical step.

1. Introduction

Gas permeation in PEMWE is important for safety [1] and efficiency [2]. At low current densities, H_2/O_2 formation rates can be lower than their permeation rates [1,3], resulting in H_2/O_2 mixing with relative concentrations within the flammability limits [4]. The O_2 permeation rate is lower [5] than that of H_2 [6], due to the permeability of O_2 being around half of that of H_2 in Nafion PEMs [3] and the recombination activity of Pt in the cathode [5]. On the other hand, H_2-in-O_2 contents in PEMWE anodes can reach the lowest explosion limit (*LEL* ≈ 4% vol. H_2-in-O_2 [4]), especially at increased cathode pressures, P_c [2,6]. To decrease the H_2-in-O_2 content, Pt electrodes [7] or Pt particles interlayers [8] have been incorporated within the PEM, oxidizing the permeated H_2 or acting as H_2/O_2 recombination catalyst, respectively. In addition, Pt coatings on the Ti-porous transport layers, PTL, can facilitate the recombination [9]. In the former cases, the H^+ resistance increases compromising PEMWE performance [7,8]. The latter approach improves the contact resistance between the anodic catalyst layer and the Ti-PTL [10], but on the expense of cost and without addressing the H_2-in-O_2 content in the catalyst layer. This was recently investigated by the addition of a thin layer with unsupported Pt alloyed with Co between the PEM and the anodic catalyst layer [11], resulting in 50% conversion of the permeated H_2 and decreasing the operating current density to 0.15 A/cm^2 without affecting the performance.

It is considered that the permeated H_2 cannot be oxidized on Ir oxide catalysts at WE operating potentials [2,7]. Very recently, the interaction of the permeated H_2 with crystalline IrO_2 was evidenced during prolonged periods at open circuit, elevated P_c and temperature (T = 80 °C), by the drop of the open circuit potential, *OCP* [12]. In the present work, the oxidation activity of IrOx oxyhydroxide anode on the permeated H_2 was investigated. Polarization measurements, involving low current densities, were acquired by simultaneously following the composition of the anode outlet gas phase by means of a thermal conductivity sensor. The results of H_2 permeation were used to apply current density and mass transport potential corrections and get mechanistic insights on the interaction of H_2 with the IrOx surface and the oxygen evolution reaction (OER).

* Corresponding author.
E-mail address: papakonstantinou@mpi-magdeburg.mpg.de (G. Papakonstantinou).

https://doi.org/10.1016/j.elecom.2019.106578
Received 26 July 2019; Received in revised form 16 October 2019; Accepted 17 October 2019
Available online 21 October 2019

2. Experimental

2.1. Cell and materials

HYDRion circular catalyst coated membranes (CCM, 63.5 cm^2, Ir based anode, Pt based cathode, N117, EW ≈ 1100, ION POWER) were recently characterized by physicochemical and electrochemical methods [13], revealing the IrOx oxyhydroxide nature of the anode catalyst. A CCM of the same batch was placed in an all Ti commercial single cell (ZE 200, Sylatech). Details on the cell and its components are given elsewhere [13,14].

2.2. Test setup

An automated test station (FuelCon 70460, Evaluator C) was used for electrochemical testing. The anode was always pumped with H_2O (0.055 μS/cm, 120 ml/min), which was re-circulated to a heated vessel (61 °C), where the first gravimetric separation step of gas/liquid phases occurred. The gas phase was mixed with N_2, and the mixture passed through a condenser to remove H_2O vapor (< 10 °C) before entering the katharometer (K1550, Hitech Instruments) for the quantification of the H_2 vol. % in the gas mixture (Fig. 1a).

The sensor measures pseudo-binary mixtures. Since the heat conductivities of N_2 and O_2 are similar (0.0262 vs. 0.02676 W/m·K at 300 K, respectively), differing by almost one order of magnitude from that of H_2 (0.182 W/m·K), the error in the calculation of the H_2 permeation flux is small (estimated ± 1.6%). This is shown in Fig. 1b, where the calibration of the katharometer with mixtures of 2 vol% H_2 in O_2 (± 2%, Westfalen AG) and N_2 under simulated experimental conditions is presented. The linear fit and the standard errors are shown in Fig. 1b, with the fitted line passing through the sensor baseline. The use of N_2 decreases by far the equilibration time of the H_2 concentration in the mixture ($t_{eq} \approx 3V_d/J$, V_d the gas phase volume ≈ 500 ml, with total volumetric flow rate 100 < J < 700 ml/min), especially at low O_2 formation rates, allowing simultaneous polarization measurements with quantification of the H_2 content in the whole current density range.

The anode inlet T was controlled and those at the middle of the anode plate and outlet were recorded (Fig. 1a). The cathode was always flowed with dry H_2 and served as pseudo-reference H_2 electrode. P_c was controlled by a back-pressure valve.

2.3. Electrochemical measurements

The cell potential and current were controlled with a 2-quadrant load (30 mA-100 A range). Solartron 1287A potentiostat and 1250B frequency response analyzer were connected in parallel to the single cell and the 2-quadrant load for chronoamperometry (CA, load disconnected) and impedance (EIS, load connected) measurements. The galvanostatic polarization curves were measured in both ascending (A) and descending (D) directions. EIS at selected current densities provided for high frequency resistance, *HFR*, free potentials, $E_{HFR\ free}$. The minimum measuring time was 2 min, extending to 5–18 min when EIS was applied, depending on the *DC* current density. These are the measuring points during which the H_2 sensor achieved stable readings.

2.4. Pressure drop method

The cathode compartment was pressurized with H_2 and isolated with on/off valves, with the anode flowed with H_2O. *Pc* was then followed over time with an attached pressure gauge (CPT 6200, Wika). Differentiation against time provides dP_c/dt vs. time. Assuming cathodic PTLs' porosity of 0.5, the void volume of the cathodic compartment is known ($V_c \approx 10.2$ ml). With the assumption of ideal gas, Eq. (1) provides the H_2 molar flux permeating the PEM.

$$dn/dt = (V_c/RT)dP_c/dt \quad (1)$$

The H_2 permeability coefficient through the PEM, $K_{p,H2}$, is calculated by Eq. (2) [15], where A is the active area, d_{PEM} the PEM thickness (210 μm for fully hydrated N117 at 60 °C) and $\Delta P = P_{H2}{}^c - P_{H2}{}^a \approx P_{H2}{}^c$. All pressures are corrected for H_2O vapor pressure at the experimental T.

$$K_{p,H2} = (d_{PEM}/A\Delta P)dn/dt \quad (2)$$

3. Results and discussion

3.1. Zero-current H_2 permeation

A representative result of the pressure drop method is depicted in Fig. 2a. The inset shows P_c vs. time and the corresponding molar flux of H_2 permeating the PEM. $K_{p,H2}$ is constant with $P_{c,H2}$ [15]. Furthermore, the $K_{p,H2}$ values (Table 1) agree well with those reported in [15,16] and references therein for one side soaked Nafion PEMs with acid or at 100% relative humidity at the respective T.

CA measurements at potentials between 1.2 and 1.4 V are depicted in Fig. 2b at P_c = 1 and 5 bar. The current density is stabilized after 1–3 min and remains stable for more than 10 min. The current density increases with P_c, complying with the increase of H_2 flux with P_c (Fig. 3). In addition, the current density agrees with the permeation rates assessed by the pressure drop and electrochemical compensation [15] methods (Table 1), indicating the oxidation of permeated H_2 at potentials close to WE onset.

To validate the results of the zero-current permeation methods summarized in Table 1, $K_{P,H2}$ is plotted in Arrhenius form (Fig. 3). The activation energy of H_2 permeation through the hydrated N117

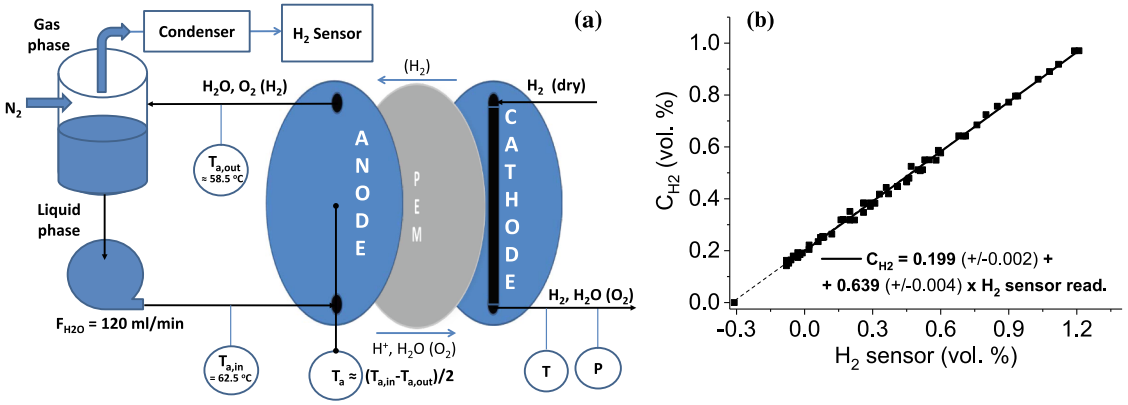

Fig. 1. (a) Schematic of the flow configuration. (b) Calibration of the H_2 sensor (min. detection limit 0.14 vol%). The cell was replaced with a pre-calibrated mass flow controller (3–100 ml/min of 2% H_2-in-O_2). The total flow rate range was 100–700 ml/min, with N_2 balance.

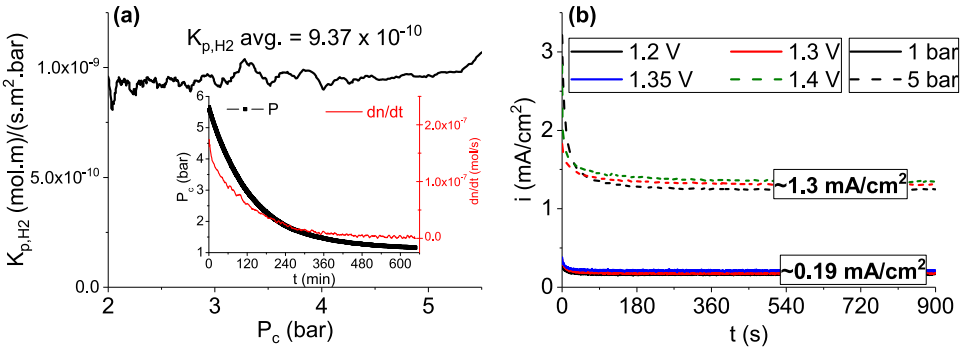

Fig. 2. (a) $K_{P,H2}$ vs. P_c by the pressure drop method at RT (inset). (b) CA measurements at potentials preceding WE onset at P_c = 1 and 5 bar (60 °C). The colors are indicated in the figures' legends.

Table 1
$K_{P,H2}$, H_2 molar fluxes and current density equivalents at different T and P_c for N117 soaked with liquid H_2O at the anode.

T (°C), P_{H2} (bar)	Method	$K_{p,H2}$		dn/dt (mol/s.m^2)	i_{H2} (mA/cm^2)
		mol/s.m.bar	Barrer		
25, 0.968	P drop	1.39×10^{-9}	41.5	6.73×10^{-6}	0.13
55, 5.03	EC comp.	2.56×10^{-9}	76.4	6.43×10^{-5}	1.24
60, 0.8	P drop	2.81×10^{-9}	83.9	1.12×10^{-5}	0.217
60, 0.8	CA	2.46×10^{-9}	73.4	9.85×10^{-6}	0.19
60, 4.8	P drop	2.81×10^{-9}	83.9	6.74×10^{-5}	1.3
60, 4.8	CA	2.81×10^{-9}	83.9	6.74×10^{-5}	1.3
80, 0.526	P drop	4.28×10^{-9}	127.8	1.13×10^{-5}	0.217

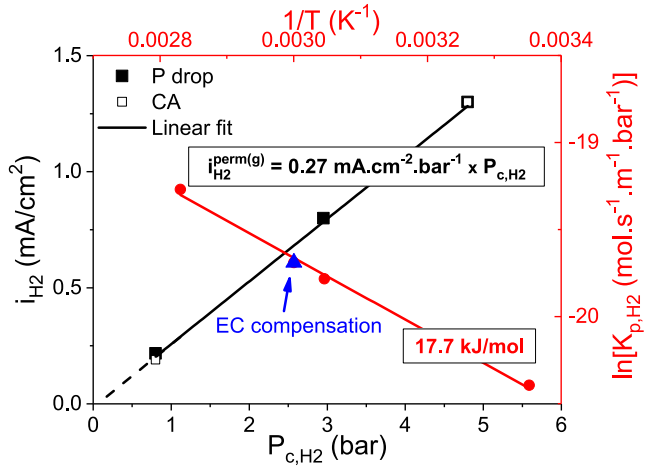

Fig. 3. The dependence of the permeated H_2 flux in current density units, on $P_{c,H2}$ (left y-axis/bottom x-axis) and Arrhenius plot of the $K_{P,H2}$ from pressure drop and electrochemical compensation methods (right y-axis/top x-axis). The colors are indicated in the figures' legends.

(17.7 kJ/mol) is in good agreement with 20 kJ/mol reported in [17]. The permeated H_2 flux, in current density units, is linear on $P_{c,H2}$ with slope 0.27 mA/cm^2/bar at 60 °C, in excellent agreement with [15], passing through the origin (Fig. 3).

3.2. H_2 permeation under current

The H_2 sensor readings, x_{H2} in vol. % in the gas mixture, are transformed into permeated H_2 current density (mA/cm^2) via Eq. (3), knowing the volumetric N_2 flow rate, J_{N2} (ml/s), and assuming 100% O_2 Faradic efficiency. F is the Faraday constant and V_m the gas molar volume.

$$i_{H2} = [2Fx_{H2}(J_{O2} + J_{N2})]/[V_m A(100 - x_{H2})] \quad (3)$$

It is shown in Fig. 4a vs. WE current density for polarization measurements in both directions at P_c = 5 bar and 60 °C. The H_2 permeation flux increases linearly with current density in accordance with [6,9,11,18,19], herein above 0.3 A/cm^2, overlapping in both measuring directions (Fig. 4a). However, the low current density permeation fluxes (≤0.1 A/cm^2) are significantly lower than the high current density intercept and the respective zero-current permeation flux (Fig. 4a and inset). The intercept of the H_2 permeation flux, measured at WE current densities higher than 0.05–0.1 A/cm^2, is reported to match the respective zero-current permeation [6,18]. The present results suggest H_2 consumption that decreases with current density/potential.

The H_2 consumption is quantified in current density units by Eq. (4), where $i_{H2,max}$ is the current density of the maximum permeation rate and $i_{H2,zcm}$ that of zero-current methods (Fig. 3 and Table 1), assuming potential dependent consumption that levels out at high current densities.

$$i_{H2,cons} = [i_{H2,zcm} + ((i_{H2,max} - i_{H2,zcm})/i_{WE,max})i_{WE}] - i_{H2,meas} \quad (4)$$

Since the permeation slope should be the lowest when free from the influence of consumption, as reference slope is taken the $(i_{H2,max} - i_{H2,zcm})/i_{WE,max}$ = 5.127 mA/A (dashed line in Fig. 4a). Then, the measured data are subtracted and the results are shown in Fig. 4b. The H_2 consumption is constant at lower than 75 mA/cm^2 current density in both directions, corresponding to 75% conversion with respect to zero-current permeation. With increasing current density the consumption decays, inherently with the present treatment. If the increase of H_2 permeation rate is stronger than linear, as observed in [8] at current densities higher than 1.5 A/cm^2 with N117 at 80 °C, this would imply increase of H_2 consumption with potential/current density in the present measurements. However, this is not likely, supported by the hysteresis in H_2 consumption between the two measuring directions in the 0.075–0.3 A/cm^2 range (Fig. 4b), which suggests hysteresis in the changes of the catalyst oxidation state and/or in the surface coverage by less reactive oxygen containing species with potential. Whether the H_2 consumption is direct electrochemical oxidation or indirect, e.g. involving H_2 adsorption with H_2O release and H_2O assisted catalyst re-oxidation driven by the applied potential, cannot be definitely discriminated. The potential dependence of H_2 consumption suggests the latter.

The H_2-in-O_2 volumetric percentage vs. current density is shown in Fig. 4c in log-log plot for better visibility, calculated by Eq. (5) for 100% O_2 Faradic efficiency.

$$H2 - in - O2 = 100J_{H2}/J_{O2} \quad (5)$$

The results in Fig. 4c are complemented with the zero-current permeation at two P_c values without accounting for consumption or permeation enhancement, as well as with the enhanced permeation at 5 bar without consumption. The H_2-in-O_2 percentage is lower by ca. 50% than that of the zero-current permeation, and the lowest current density at which the H_2-in-O_2 *LEL* is not exceeded decreases from 65 to

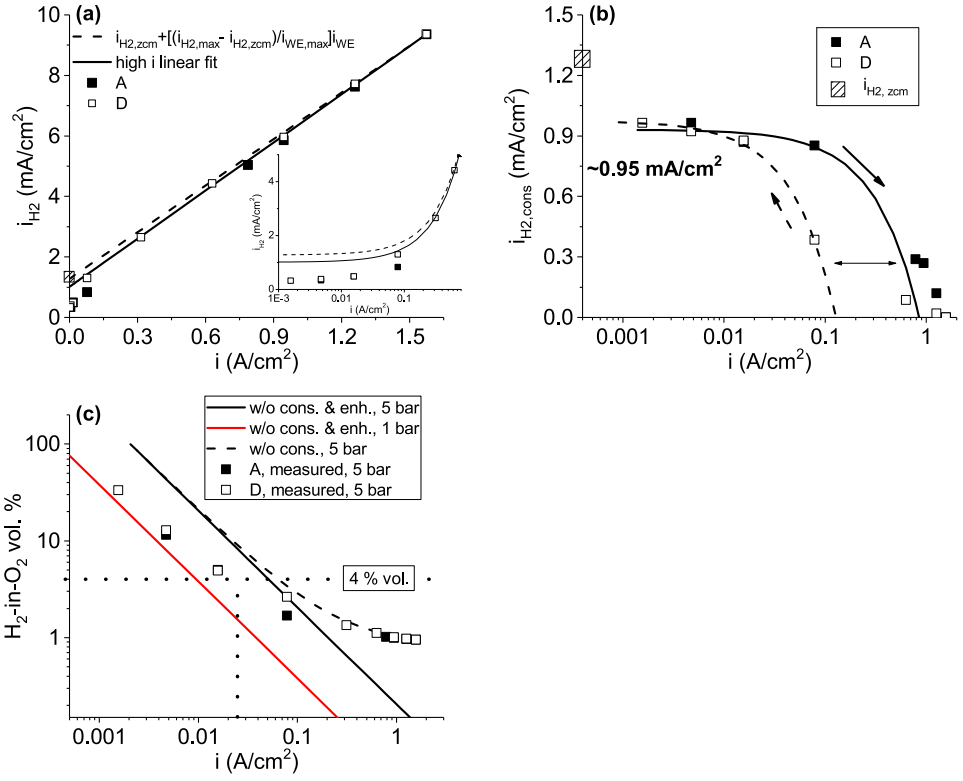

Fig. 4. (a) Permeated H_2 flux in current density units vs. WE current density during polarization measurements in ascending (A) and descending (D) directions at 5 bar (60 °C). The solid line is the high current density linear fit. The dashed line connects the maximum permeation flux with the zero current permeation. Zoom-in at low current densities in log scale in the inset. (b) The consumed H_2 flux in current density units vs. WE current density in log scale. The shaded symbol is the zero-current permeation. (c) H_2-in-O_2 vol. % vs. WE current density in log-log scales. The points are the measured values at 5 bar. The solid lines indicate the zero-current permeation without consumption or permeation enhancement at $P_c = 1$ and 5 bar. The dashed black line corresponds to the enhanced permeation without consumption at 5 bar. Colors and symbols are indicated in figures' legends.

25 mA/cm^2.

3.3. Performance analysis

Descending polarization curves at three P_c values are presented in Fig. 5a, as $E_{HFR\ free}$ vs. current density in log scale. The $E_{HFR\ free}$ difference between ambient and increased pressure below ca. 0.25 A/cm^2 matches the difference due to the nominal $P_{c,H2}$ by the Nernst equation (Eq. (6)).

$$\eta(T, P) = E_{HFRfree} - E_{rev}(T) - (RT/2F)ln(P_{a,O2}^{0.5} P_{c,H2}) \quad (6)$$

This results in the full overlap of the respective curves, when plotted as T and $P_{c,H2}$ corrected WE overpotential, $\eta(T,P)$ (Fig. 4a), calculated by Eq. (6). Liquid H_2O is considered incompressible and its activity is assumed as unity and thus omitted in Eq. (6). For T corrections of the reversible potential (Eq. (7)) [20], to account for T increase at current density > 0.3 A/cm^2, the T of the anode plate is used, which is always equal or very close to the average value of T at the anode inlet and outlet (Fig. 1a).

$$E_{rev}(T) = (1/2F)(-159.6T + 2.847 \cdot 10^5) \quad (7)$$

Excellent linearity with current density in log scale is observed up to 50 mA/cm^2 (slope = 32 mV/d, Fig. 5a). At higher current densities, all curves bend up suggesting mass transport contributions [21]. The effect of pressure on mass transport is weak in the herein used P_c and current density ranges (up to 5 bar and 1.575 A/cm^2), seen as decrease of $\eta(T,P)$ by 5–6 mV at the highest current density and 5 bar with respect to ambient pressure.

The agreement of the measured $E_{HFR\ free}$ vs. $P_{c,H2}$ (Fig. 4a) and the linear dependence of zero-current permeation on P_c (Section 3.1) motivated potential corrections for a cathodic mass transport-driven [18] H_2 pressure enhancement. The linear increase of the H_2 permeation flux with current density has been attributed to P enhancement in the cathodic catalyst layer [2,9] or supersaturated dissolved H_2 in the respective ionomer/aqueous phases [6,18]. The driving force is mass transport resistance, recently linked with the ionomer content [18]. In a simplified approach, Henry's law, $C_{H2(l)} = S_{H2} \cdot P_{H2(g)}$, states the proportionality of the gas partial pressure with the dissolved gas concentration via the solubility, S_{H2}. In the P enhancement concept, S_{H2} is kept constant and $C_{H2(l)}$ and $P_{H2(g)}$ increase proportionally, whereas in the supersaturation concept, $P_{H2(g)}$ is constant and $C_{H2(l)}$ and S_{H2} vary accordingly. Based on poroelectroelastic theory, capillary pressures

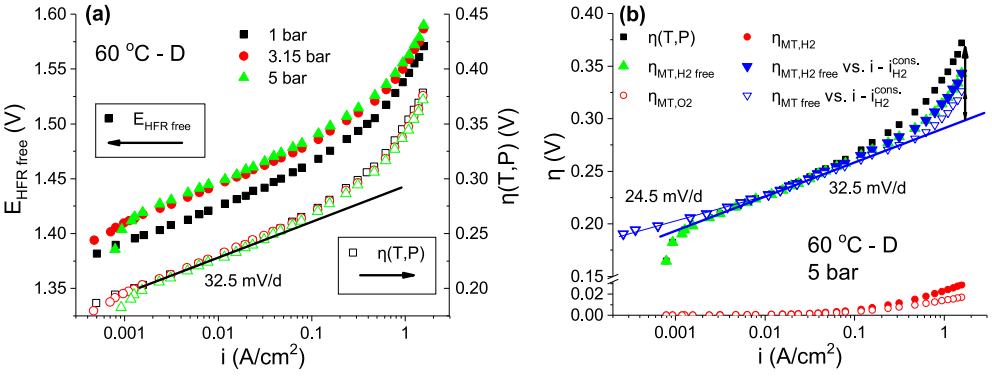

Fig. 5. (a) $E_{HFR\ free}$ (left-y axis) and $\eta(T,P)$ (right y-axis) vs. current density in log scale cathodic polarization curves at P_c = 1, 3.15 and 5 bar (60 °C). (b) $\eta(T,P)$ (black squares), $\eta_{MT,H2}$ (red circles), $\eta_{MT,H2\ free}$ (green triangles) with current density correction for H_2 consumption (blue triangles), $\eta_{MT,O2}$ (red open circles) and $\eta_{MT\ free}$ (blue open triangles) vs. current density in log scale (5 bar, 60 °C). (For interpretation of the references to colour in this figure legend, the reader is referred to the web version of this article.)

higher than 100 bar have been estimated in the filled with liquid H_2O Nafion pores [22]. In addition, the pressure exerted by the dissolved gas will influence the total H_2O pressure [23], affecting the swelling properties of the ionomer phase and the transport properties. In addition, *T* effects at high current densities due to overheating may change the swelling and hence affect the transport. This can explain the stronger than linear H_2 permeation increase at current densities higher than 1.5 A/cm^2 observed in [8]. This is not observed herein, in accordance with other reports [6,9,18], even involving current densities up to 3–5 A/cm^2 [11,19], possibly due to relatively short times at high polarization (max. 5 min at each current density).

The in-depth analysis at the nanoscale of the origin of the apparently linear permeation enhancement with $P_{c,H2}$ (Fig. 3) [1,15] and WE current density (Fig. 4a) [6,9,11,18,19] is beyond the scope of the present work. In a simplified and in average approach at the macroscale, we proceed with the analysis with the *P* enhancement concept, since the mathematical treatment is similar to the supersaturation concept, as mentioned above. The linear correlation of the H_2 permeation flux with current density can be represented by Eq. (8), with the intercept corresponding to the nominal $P_{c,H2}$.

$$P_{c,H2}(i) = P_{c,H2}(0) + f_P\, i_{WE} \tag{8}$$

The slope of the H_2 permeation flux in current density units, $i_{H2}^{perm(g)}$, vs. $P_{c,H2}$, provided by the zero-current methods ($i_{H2}^{perm(g)}/P_{c,H2} = 0.27$ mA/cm^2/bar, Fig. 3) is used to quantify the P enhancement factor, f_P, by Eq. (9), accounting for diffusive permeation due to P_{H2} gradient across the PEM [2,9,15].

$$f_P = [i_{H2}(i)/i_{WE}]/[i_{H2}^{perm(g)}/P_{c,H2}] \tag{9}$$

The cathodic mass transport potential, $\eta_{MT,H2}$, is computed by the Nernst equation (Eq. (10)).

$$\eta_{\mathrm{MT,H2}} = (RT/2F)ln[(P_{c,H2}(0) + f_P i_{WE})/P_{c,H2}(0)] \tag{10}$$

To avoid the influence of H_2 consumption that virtually increases H_2 permeation slope (Fig. 4a), the slope of 5.127 mA/A (dashed line in Fig. 4a) is used, providing $f_P = 19$ bar/A/cm^2, in good agreement with [2,9].

The corrections for $\eta_{MT,H2}$ at $P_c = 5$ bar are shown in Fig. 5b. The curves' bending (Fig. 5a) coincides with the onset of the $\eta_{MT,H2}$ contributions (Fig. 5b), accounting for ca. 30 mV at the maximum current density. Their subtraction from $\eta(T,P)$ extends the Tafel line to 0.2 A/cm^2, signifying the transition to another mass transport mode, e.g. anodic.

Subsequently, the WE current density is corrected for the H_2 consumption (Fig. 4b), accounting for mixed potential, evident by the downward bending at extremely low current densities (< 3–5 mA/cm^2, Fig. 5), and assuming electrochemical oxidation of the permeated H_2, supported by the CA results at potentials slightly preceding the OER onset (Fig. 2b). The H_2 consumption current density is subtracted, as proposed in [24], and commonly applied in PEMFCs [25], generating a Tafel slope of 24.5 mV/d for more than one decade of current density (Fig. 5b), and without affecting the slope at intermediate current densities, due to the one order of magnitude difference between H_2 permeation and O_2 formation rates ($i_{WE} > 10$ mA/cm^2).

To corroborate further the mass transport influence and accounting for the half permeability coefficient of O_2 than that of H_2 [3] and the reaction stoichiometry, four times higher current density for the appearance of mass transport resistance in the anode with respect to the cathode is expected, assuming similar anode catalyst layer structure with that of the cathode and analogous O_2 transport properties [5] with those of H_2. The upward bending of the $\eta_{MT,H2\ free}$ indeed occurs at four times higher current density than in the $\eta(T,P)$ curve (0.2 vs. 0.05 A/cm^2, respectively, Fig. 5). Hence, additional corrections for anodic mass transport-driven O_2 pressure enhancement are applied (Eq. (11)), with $f_{P,O2} \approx f_{P,H2}/4$.

$$\eta_{\mathrm{MT,O2}} = (RT/4F)ln[(P_{a,O2}(0) + f_P i_{WE})/P_{a,O2}(0)] \tag{11}$$

The Tafel region is further extended up to 0.5 A/cm^2 (Fig. 5b). The upward bending can be assigned to mass transport due to PTLs [26] and/or the kinetic influence of the OER on the IrOx surface. The mass transport potential contributions due to *P* enhancement in the catalyst layers account for 62% of the total deviation from the Tafel line.

A Tafel slope of 32.5 mV/d corresponds to a transfer coefficient $\alpha \approx 2$ at 60 °C, characteristic of a chemical step as rds [27]. Higher current densities could not be attained, due to current limitations, and limiting current, inherent with chemical rds [27], is not clearly observed (Fig. 5). The low Tafel slopes observed herein contradict the values commonly observed in literature, 40–60 mV/d [28], but the intermediate current density slope agrees with 34–36 mV/d at 80 °C, reported very recently with metallic Ir electrodes and similar cathodic mass transport corrections [18]. These values signify that the rds is a chemical step [27], possibly involving (hydro)peroxo-type radicals as OER intermediates that are electron deficient [29] and hence very reactive with H_2 [30], comprehending the observed consumption of H_2.

4. Conclusions

Quantification of the gaseous effluents of operating PEMWEs in the whole current density range provides valuable information on the underlying transport processes and mechanistic insights on the OER. The permeated H_2 is effectively consumed at low current densities on the IrOx oxyhydroxide surface, decreasing the lowest current density at which the H_2-in-O_2 *LEL* is not exceeded to 25 mA/cm^2. 62% of the deviation from the Tafel line is contributions from mass transport resistances in the catalyst layers. The rest comes from the PTLs and/or kinetic effect of the OER rds, which is suggested to be a chemical step. Further experiments and physicochemical analysis are underway to investigate the IrOx capability of consuming the permeated H_2 at higher cathode pressures and different temperatures and the IrOx structural and chemical changes imposed by the permeated H_2, respectively.

Declaration of Competing Interest

The authors declare that they have no known competing financial interests or personal relationships that could have appeared to influence the work reported in this paper.

Acknowledgements

The MAXNET Energy Consortium of the Max Planck Society and Deutsche Forschungsgemeinschaft (Grant no. SU189/7-1) are acknowledged for the financial support. Mrs X. Qu is thanked for her assistance in electrochemical testing and Mr A. Phuc Dam, Dr. T. Vidakovic-Koch and Dr. A. Zinser for the fruitful discussions.

References

[1] F. Barbir, Solar Energy 78 (2005) 661–669, https://doi.org/10.1016/j.solener.2004.09.003.
[2] M. Schalenbach, M. Carmo, D.L. Fritz, et al., Int. J. Hydrogen Energy 38 (2013) 14921–14933, https://doi.org/10.1016/j.ijhydene.2013.09.013.
[3] T. Sakai, H. Takenaka, N. Wakabayashi, et al., J. Electrochem. Soc. 132 (1985) 1328–1332, https://doi.org/10.1149/1.2114111.
[4] V. Schroeder, B. Emonts, H. Janssen, et al., Chem. Eng. Technol. 27 (2004) 847–851, https://doi.org/10.1002/ceat.200403174.
[5] P. Trinke, B. Bensmann, R. Hanke-Rauschenbach, Electrochem. Commun. 82 (2017) 98–102, https://doi.org/10.1016/j.elecom.2017.07.018.
[6] P. Trinke, P. Haug, J. Brauns, et al., J. Electrochem. Soc. 165 (2018) F502–F513, https://doi.org/10.1149/2.0541807jes.
[7] M. Schalenbach, D. Stolten, Electrochim. Acta 156 (2015) 321–327, https://doi.org/10.1016/j.electacta.2015.01.010.
[8] C. Klose, P. Trinke, T. Boehm, et al., J. Electrochem. Soc 165 (2018) F1271–F1277, https://doi.org/10.1149/2.1241814jes.
[9] H. Ito, N. Miyazaki, M. Ishida, et al., Int. J. Hydrogen Energy 41 (2016) 20439–20446, https://doi.org/10.1016/j.ijhydene.2016.08.119.

[10] C. Rakousky, U. Reimer, K. Wippermann, et al., J. Power Sources 326 (2016) 120–128, https://doi.org/10.1016/j.jpowsour.2016.06.082.
[11] N. Briguglio, S. Siracusano, G. Bonura, et al., Appl. Catal. B: Environ. 246 (2019) 254–265, https://doi.org/10.1016/j.apcatb.2018.12.079.
[12] A. Weiss, A. Siebel, M. Bernt, et al., J. Electrochem. Soc. 166 (2019) F487–F497, https://doi.org/10.1149/2.0421908jes.
[13] G. Papakonstantinou, G. Algara-Siller, D. Teschner, et al., submitted to Appl. Catal. B: Environ.
[14] C. Immerz, M. Paidar, G. Papakonstantinou, et al., J. Appl. Electrochem. 48 (2018) 701–711, https://doi.org/10.1007/s10800-018-1178-2.
[15] B. Bensmann, R. Hanke-Rauschenbach, K. Sundmacher, Int. J. Hydrogen Energy 39 (2014) 49–53, https://doi.org/10.1016/j.ijhydene.2013.10.085.
[16] D. Bessarabov, PEM Fuel Cell Diagnostic Tools, CRC Press, Boca Raton, 2012, pp. 443–473.
[17] M. Schalenbach, T. Hoefner, P. Paciok, et al., J. Phys. Chem. C 119 (2015) 25145–25155, https://doi.org/10.1021/acs.jpcc.5b04155.
[18] P. Trinke, G.P. Keeley, M. Carmo, et al., J. Electrochem. Soc. 166 (2019) F465–F471, https://doi.org/10.1149/2.0171908jes.
[19] D. Bessarabov, A.J. Kruger, S.M. Luopa, et al., ECS Trans. 75 (14) (2016) 1165–1173, https://doi.org/10.1149/07514.1165ecst.
[20] I. Barin, G. Platzki, Thermochemical data of pure substances, 3rd ed.; 1995, p. 797–796. Weinheim.
[21] M. Bernt, H.A. Gasteiger, J. Electrochem. Soc. 163 (2016) F3179–F3189, https://doi.org/10.1149/2.0231611jes.
[22] M.H. Eikerling, P. Berg, Soft Matter 7 (2011) 5976–5990, https://doi.org/10.1039/c1sm05273j.
[23] A.A. Kalinnikov, S.A. Grigoriev, D.G. Bessarabov, Int. J. Hydrogen Energy 44 (2019) 7889–7904, https://doi.org/10.1016/j.ijhydene.2019.02.025.
[24] C. Mittelsteadt, T. Norman, M. Rich, et al., in: P.T. Moseley, J. Garche (Eds.), Electrochemical Energy Storage for Renewable Sources and Grid Balancing, Elsevier, 2015, pp. 159–181.
[25] H.A. Gasteiger, S.S. Kocha, B. Sompalli, et al., Appl. Catal. B: Environ. 56 (2005) 9–35, https://doi.org/10.1016/j.apcatb.2004.06.021.
[26] T. Schuler, T.J. Schmidt, F.N. Buechi, J. Electrochem. Soc. 166 (2019) F555–F565, https://doi.org/10.1149/2.1241908jes.
[27] J. O'm Bockris, J. Chem. Phys. 24 (1956) 817–827, https://doi.org/10.1063/1.1742616.
[28] T. Reier, H.N. Nong, D. Teschner, et al., Adv. Energy Mater. 7 (2017) 1601275, https://doi.org/10.1002/aenm.201601275.
[29] V. Pfeifer, T.E. Jones, S. Wrabetz, et al., Chem. Sci. 7 (2016) 6791–6795, https://doi.org/10.1039/C6SC01860B.
[30] C. Massue, V. Pfeiffer, X. Huang, et al., Chem. Sustain. Chem. 10 (2017) 1943–1957, https://doi.org/10.1002/cssc.201601817.